nature materials

ARTICLES

PUBLISHED ONLINE: 26 JULY 2009 | DOI: 10.1038/NMAT2505

Comparative materials differences revealed in engineered bone as a function of cell-specific differentiation

Eileen Gentleman[1,2], Robin J. Swain[1], Nicholas D. Evans[1,2], Suwimon Boonrungsiman[1,2], Gavin Jell[1,2], Michael D. Ball[1,2], Tamaryn A. V. Shean[3], Michelle L. Oyen[3], Alexandra Porter[1] and Molly M. Stevens[1,2]*

An important aim of regenerative medicine is to restore tissue function with implantable, laboratory-grown constructs that contain tissue-specific cells that replicate the function of their counterparts in the healthy native tissue. It remains unclear, however, whether cells used in bone regeneration applications produce a material that mimics the structural and compositional complexity of native bone. By applying multivariate analysis techniques to micro-Raman spectra of mineralized nodules formed *in vitro*, we reveal cell-source-dependent differences in interactions between multiple bone-like mineral environments. Although osteoblasts and adult stem cells exhibited bone-specific biological activities and created a material with many of the hallmarks of native bone, the 'bone nodules' formed from embryonic stem cells were an order of magnitude less stiff, and lacked the distinctive nanolevel architecture and complex biomolecular and mineral composition noted in the native tissue. Understanding the biological mechanisms of bone formation *in vitro* that contribute to cell-source-specific materials differences may facilitate the development of clinically successful engineered bone.

Disease and injury so severe that the body cannot heal naturally necessitate clinical intervention to restore a level of tissue function. One aim of regenerative medicine is to meet this need with laboratory-grown constructs that can be surgically implanted, as they may avoid many problems associated with allogenic and autogenic grafts such as limited availability[1], immune compatibility[2], and disease transmission[3]. Central to such strategies is the re-establishment of tissue functionality by way of tissue-specific cells contained within the constructs, be they somatic, genetically reprogrammed or adult/embryo-derived stem cells. Whether they contract synchronously in the case of cardiac tissue, translate sound vibrations to electrical signals as in the inner ear or produce load-bearing extracellular matrix (ECM) as in connective tissues such as bone, the primary determinant of success of a regenerative medicine therapy will invariably be dependent on whether or not the cells replicate the functionality of their counterparts in the healthy tissue.

It is particularly challenging to isolate and culture functional tissue-specific cells in sufficient quantities to provide effective therapies. Owing to their unlimited self-renewal capacity and plasticity potential, embryonic stem cells (ESC; refs 4, 5) have attracted widespread interest and have recently gained FDA approval for human trials[6]. However, ethical and safety issues remain because of their potential for tumour formation[7]. Stem cells derived from adult tissues such as bone marrow, which are currently being investigated in over 700 clinical trials in the US (ref. 8), avoid many issues that may preclude ESC use, but may lack their unlimited proliferation potential. In addition, both embryonic and adult stem cells may need to undergo directed differentiation before use and the efficacy of available protocols remains controversial. It is also often difficult to determine whether cells are functioning as they would in the native tissue. Researchers use a combination of molecular markers, gene expression and histological stains, but many methods fail to assess global biochemical, mechanical and structural properties that determine cell and tissue function.

Bone is a prime target for regenerative medicine therapies with over two million replacement procedures carried out annually worldwide[9]. Bone is also an ideal tissue for investigating cell sources for regenerative medicine, as cells derived from bone, adult stem cells and ESC have all been reported to form mineralized, bone-like nodules *in vitro*[10–13]. Despite this, a detailed comparative understanding of the biological activities, architecture, mechanical properties and biochemical/material composition of these nodules is still elusive. In the body, bone develops through a tightly regulated process leading to a hierarchically ordered, three-dimensional structure[14]. It is unclear how similar the mineralized material formed from cells cultured *in vitro* is to native bone.

Here we formed mineralized nodules *in vitro* from mouse ESC, neonatal calvarial osteoblasts (OB) and adult bone-marrow-derived mesenchymal stem cells (MSC) and compared them with one another and native bone using a combination of materials and biological characterization methods. Our results reveal clear differences in the bone-like material formed. They also provide insight into the biological mechanisms that drive these processes, and highlight the importance of cell source in regenerative medicine.

To compare mineralized nodules formed by ESC, OB and MSC, we grew them in osteogenic medium for 28 days. All three cell types formed dense structures described in the literature as 'bone nodules'[10–12]; however, the nodules appeared different on visual inspection. ESC formed nodules quickly from highly confluent multilayered regions that developed into dense mineralized

[1]Department of Materials; [2]Institute of Biomedical Engineering, Imperial College London, London SW7 2AZ, UK, [3]Cambridge University Engineering Department, Cambridge CB2 1PZ, UK. *e-mail: m.stevens@imperial.ac.uk.

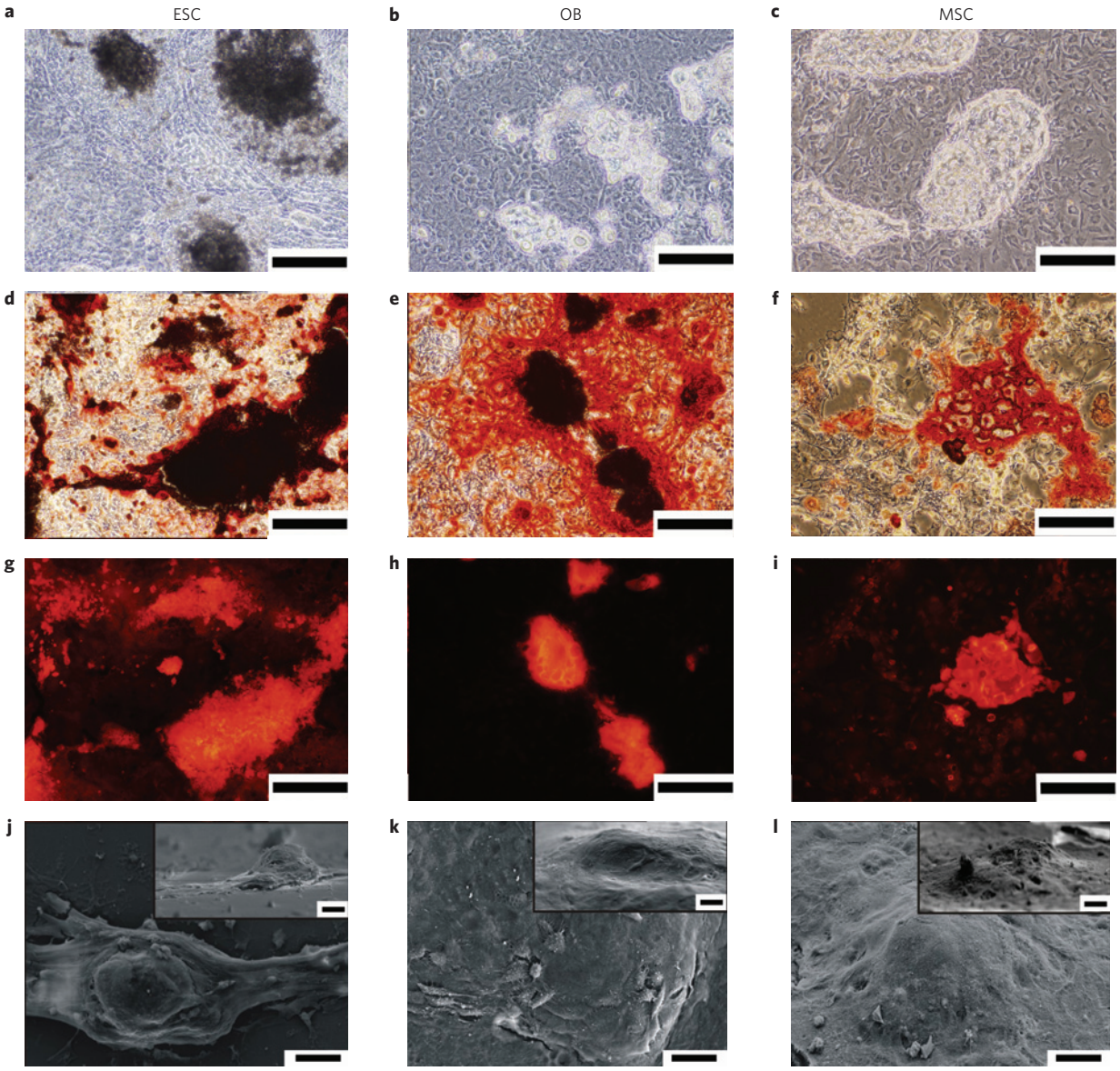

Figure 1 | Mineralized nodules formed from three different cell sources analysed by standard microscopy techniques. Mineralized nodules formed from ESC (**a**,**d**,**g**,**j**), OB (**b**,**e**,**h**,**k**) and MSC (**c**,**f**,**i**,**l**) after 28 days in culture. **a**–**c**, Phase contrast images of ESC nodules appear dark whereas those from OB and MSC are bright. **d**–**f**, The calcium stain, ARS, is positive on nodules from all three cell sources. **g**–**i**, ARS stained nodules observed using epifluorescence microscopy (excitation 510–560 nm, emission >590 nm) further confirm the presence of calcium-containing mineral in all cultures. (Scale bars in **a**–**i** represent 200 μm.) **j**–**l**, SEM micrographs showing large dense nodule structures raised from the culture surface (scale bars in **j**–**l** represent 10 μm).

structures (Fig. 1a). In contrast, OB and MSC formed nodules more slowly and in discrete patches, preceded by cellular aggregation before mineralization (Fig. 1b,c). Despite these differences, all nodules stained positive for Alizarin Red S (ARS), a histological stain used to detect calcified tissue by its chelation with calcium (Fig. 1d–f,g–i). Scanning electron microscopy (SEM) revealed that the nodules were between 100 μm and 1.5 mm in diameter and raised from the culture surface by as much as 150 μm (Fig. 1j–l). Using energy-dispersive X-ray (EDX) spectroscopy, we identified Ca and P peaks in spectra of mineralized nodules from all three cell sources (data not shown), with Ca:P ratios similar to those observed in native bone[15]. However, we could not detect consistent differences between nodules using either of these techniques. Standard biological techniques such as morphological and histological analyses thereby supplied limited distinguishable information between nodules, indicating a more systematic, materials-based analytical approach was necessary.

Mineralization was not apparent during the first two weeks of culture, so dense cellular/proteinaceous aggregates, which precede nodule formation, were examined instead. Analyses were carried out on live cell cultures using micro-Raman spectroscopy—a non-destructive technique based on the inelastic scattering of light by chemical bonds, which can be used to determine the biomolecular composition of cells or tissues by the relative intensities of characteristic molecular vibrations[16].

Raman spectra of ESC before mineralization were dominated by protein features and peaks indicative of nucleic acids and phospholipids (Fig. 2a), suggesting that premineralized ESC nodules consisted of cells combined with a proteinaceous matrix. In contrast, spectra from premineralized OB and MSC revealed weaker nucleic acid and phospholipid signatures, and were dominated by different protein spectral features than ESC. The spectral regions detected in OB and MSC were similar to those observed in spectra of standards created from type-II collagen[17],

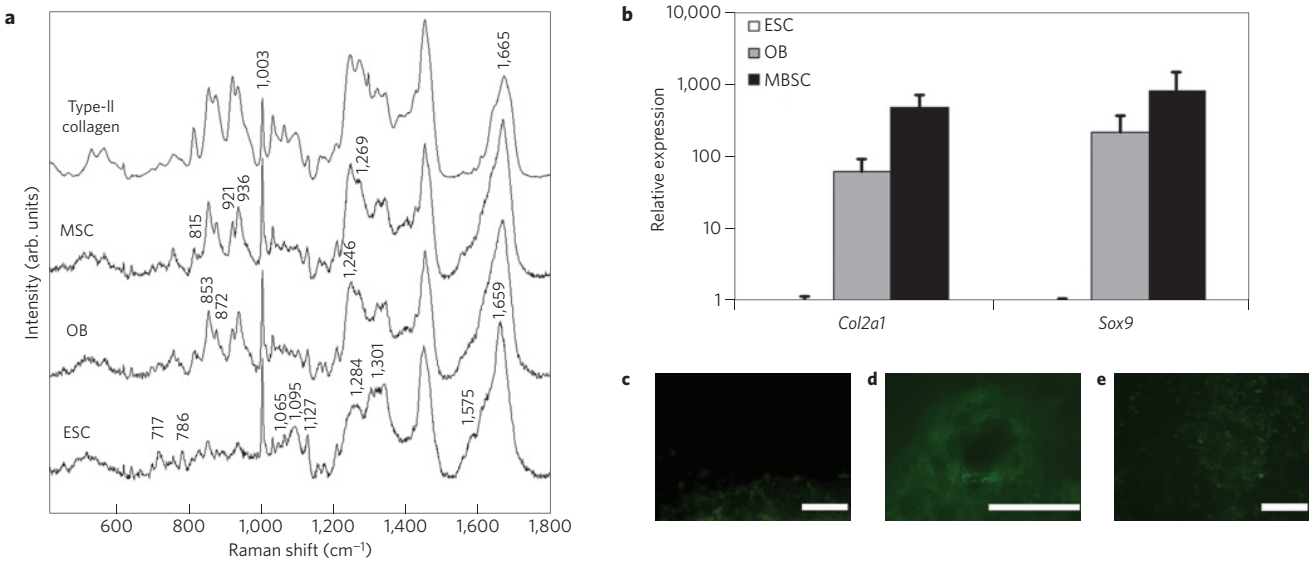

Figure 2 | Raman spectroscopy, immunostaining and gene expression evidence for type-II collagen in differentiating cultures. a, Raman spectra of premineralization ESC, OB and MSC nodules plotted with the spectrum of type-II collagen standards. ESC spectra were marked by protein features including the amide I band (1,659 cm^{-1}), skeletal C–C vibrations (936 cm^{-1}) and amide III vibrations (1,284 cm^{-1}; ref. 41). Peaks indicative of nucleic acids (786, 1,095, 1,575 cm^{-1}) and bands corresponding to phospholipids (717, 1,065, 1,127, 1,301 cm^{-1}; ref. 42) were also apparent. OB and MSC spectra had weaker nucleic acid and phospholipid signatures, and different protein spectral features than ESC including C–C backbone stretch (815 cm^{-1}), skeletal C–C vibrations (936 cm^{-1}), C–N–H amide III stretch (1,246 and 1,269 cm^{-1}) and molecular vibrations in tyrosine (853 cm^{-1}), hydroxyproline (872 cm^{-1}) and proline (921 cm^{-1}; ref. 17). **b**, Mean relative expression (and s.d.) compared with the expression of ESC at the same time point determined by quantitative real-time reverse-transcriptase polymerase chain reaction (RT-PCR) of genes *Col2a1* (type-II collagen) and *Sox9* (a transcription factor necessary for cartilage formation) in premineralization cultures of ESC, OB and MSC. Note that the *y* axis is a logarithmic scale. ($n \geq 3$.) **c**–**e**, Immunostaining for type-II collagen in cultures of ESC (**c**), OB (**d**) and MSC (**e**) after 14 days in culture. The scale bar in **c**, **d** and **e** is 200 μm.

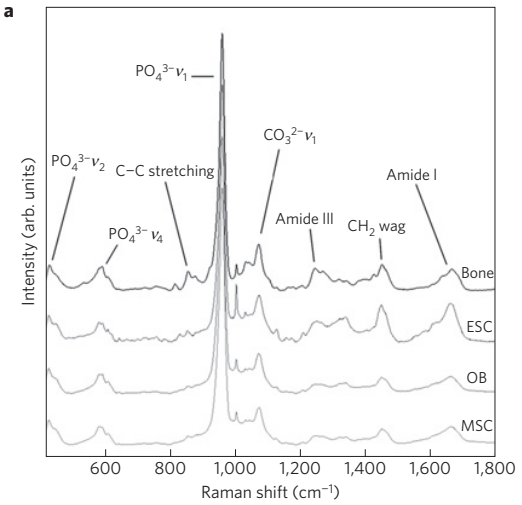

b

	Phosphate peak			
	Position (cm^{-1})	FWHM (cm^{-1})	Mineral to matrix ratio	Carbonate to phosphate ratio
Bone ($n = 44$)	960.3 ± 0.1	16.8 ± 0.3	3.81 ± 0.42	0.16 ± 0.02
ESC ($n = 80$)	960.3 ± 0.2	16.5 ± 0.6*	2.47 ± 1.31*‡§	0.22 ± 0.08*‡§
OB ($n = 87$)	959.9 ± 0.3*†§	17.9 ± 1.0*†	6.58 ± 2.68*	0.16 ± 0.08§
MSC ($n = 53$)	960.4 ± 0.2	17.6 ± 0.4*†	6.26 ± 1.53*	0.12 ± 0.02*

Figure 3 | Raman spectra of mineralized nodules and native bone, and their properties as determined by univariate peak analysis. a, Raman spectra of native mouse bone, ESC, OB and MSC after 28 days in culture. Notice that the Raman spectra of mineralized nodules are similar to one another and to native bone. The PO_4^{3-} ν_1 symmetric stretch near 960 cm^{-1} dominates the spectra of all four materials. Peaks associated with the substituted CO_3^{2-} ν_1 in-plane vibrations near 1,070 cm^{-1} are also evident. Lower-intensity vibrations corresponding to the ν_2, ν_3 (1,020–1,100 cm^{-1}) and ν_4 phosphate modes are apparent. Prominent protein bands, such as the amide I mode (1,595–1,720 cm^{-1}) and amide III envelope (1,243–1,269 cm^{-1}) are also visible. Spectra are scaled to represent equal PO_4^{3-} ν_1 peak intensity. ESC matrix peaks between 1,200 and 1,720 cm^{-1} seem stronger than those of the other materials because ESC had the lowest mineral to matrix ratio. **b**, Table detailing the phosphate peak (PO_3^{4-} ν_1) parameters and mineral properties as determined by univariate peak analysis carried out by curve fitting Raman spectra of day-28 mineralized nodules. *n* represents the number of spectra recorded for each group. A Kruskal–Wallis ANOVA was used to determine statistical significance ($p < 0.05$) combined with a Mann–Whitney test with Bonferroni correction to determine statistical significance between individual groups. Statistically significant difference between Sample X and *native bone, † ESC, ‡ OB and § MSC.

the main protein constituent of cartilage and a precursor for bone mineralization in the embryonic skeleton. Analysis of the spectral covariance matrix[18] revealed correlation coefficients of 0.96 for both OB and MSC when compared with type-II collagen standards (computed over the 415–1,600 cm^{-1} spectral range). These characteristic peaks were not observed in ESC spectra, and correlation coefficients suggested they were less similar to type-II collagen standards ($R = 0.85$).

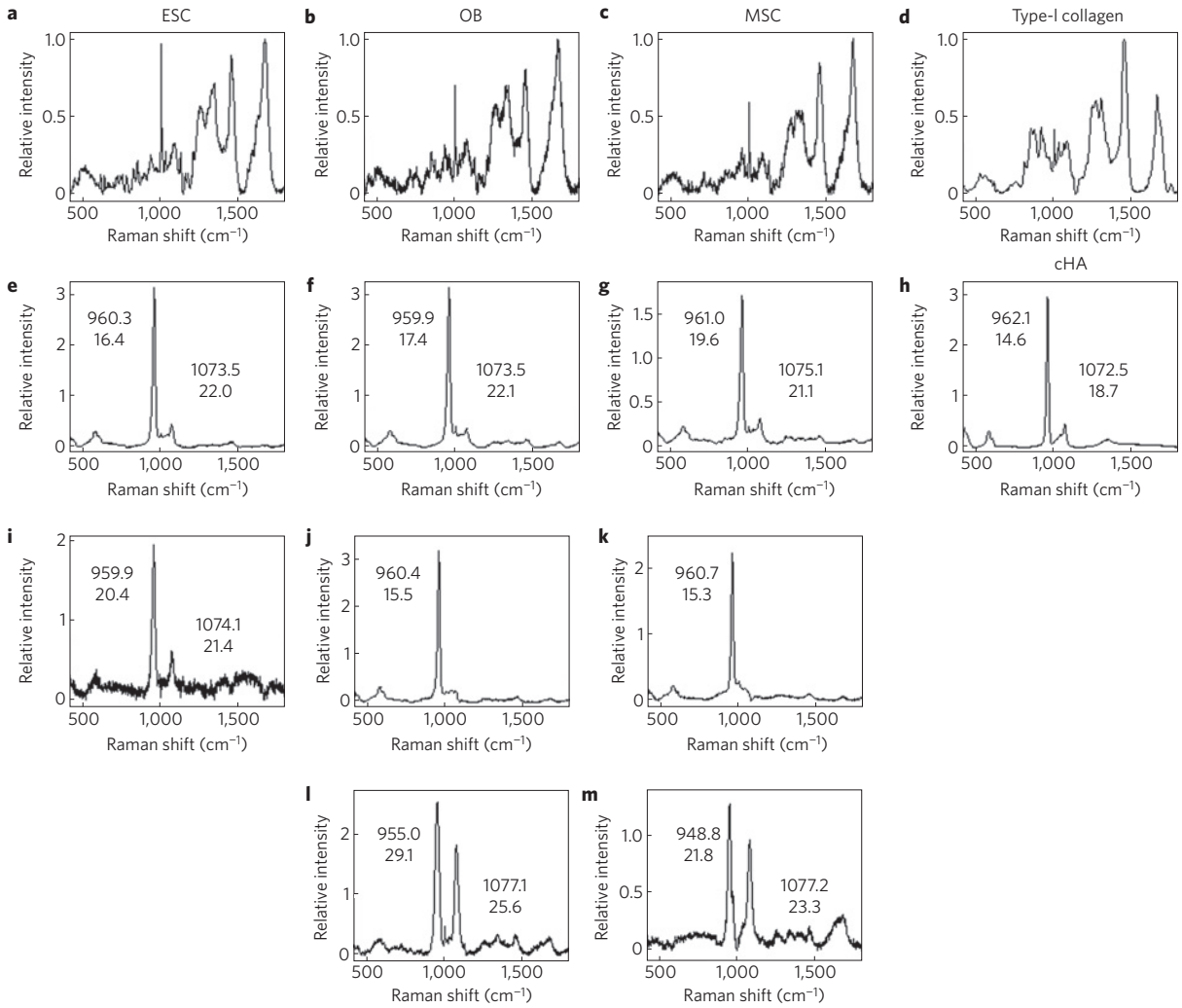

Figure 4 | Factor analyses of mature mineralized nodules after 28 days in culture. a–c, Matrix factors describing the proteinaceous component of mineralized nodules for ESC, OB and MSC. **e–g**,**i–m**, Mineral factors generated for ESC (**e**,**i**), OB (**f**,**j**,**l**) and MSC (**g**,**k**,**m**). The peak positions and full-widths at half-maximum (FWHM) for the PO_4^{3-} ν_1 and CO_3^{2-} ν_1 peaks are noted. **d**,**h**, Raman spectra of type-I collagen (**d**) and synthetic cHA (**h**) for comparison. Note the similarities between the matrix factors (**a**,**b**,**c**) and type-I collagen, which contains peaks corresponding to the C–C backbone stretch at 815 cm^{-1}, proline and hydroxyproline bands at 853, 872 and 921 cm^{-1}, and amide I near 1,665 cm^{-1}. Spectra of cHA standards show similarities to the carbonate-substituted apatite mineral factors in mineralized nodules (**e–g**), with the exception that the PO_4^{3-} ν_1 band in cHA is shifted to a higher wavenumber and has a lower FWHM, indicating that it is more crystalline.

To further confirm the presence of type-II collagen in premineralized OB and MSC cultures and its absence in ESC, we immunostained day 14 cultures with antibodies to type-II collagen. Although OB and MSC showed clear staining in cell-protein aggregates (Fig. 2d,e), we found no indication of type-II collagen in ESC (Fig. 2c). Real-time RT-PCR, a technique used to quantify the expression of genes indicative of a particular cell phenotype, confirmed this result. Although expression of *Col2a1*, the gene for type-II collagen, increased by a factor of 3.45 ± 0.33, and *Sox9* (a gene essential for cartilage formation[19]) by a factor of 4.73 ± 0.37 in ESC between plating and premineralization, OB and MSC expressed 63 and 501 times more *Col2a1* and 219 and 829 times more *Sox9*, respectively, compared with ESC (Fig. 2b). These differences suggest that a type-II collagen intermediary precedes mineralized nodule formation in OB and MSC but not in ESC.

By day 28, ESC, OB and MSC cultures all contained mineralized nodules, and we did not detect Raman spectral peaks indicative of type-II collagen. Indeed as cultures mineralized, expression of *Col2a1* decreased in OB and MSC (see Supplementary Fig. S1). Raman spectra of mature mineralized nodules instead revealed bands characteristic of native bone (Fig. 3a), with correlation coefficients ≥ 0.99 (mineralized nodules compared with native bone). Spectra of both native bone and mineralized nodules were dominated by the PO_4^{3-} ν_1 symmetric stretch near 960 cm^{-1} and weaker peaks associated with the substituted CO_3^{2-} ν_1 in-plane vibrations near 1,070 cm^{-1} (ref. 20). These peaks correspond to the mineral component of bone, hydroxyapatite $Ca_{10}(PO_4)_6(OH)_2$, into which carbonate CO_3^{2-} can substitute for the OH^- and/or PO_4^{3-} groups. *In vivo*, bone mineral is deposited on an ECM composed predominately of type-I collagen. Raman spectra of mineralized nodules and native bone reflected their proteinaceous component and were marked by prominent protein bands corresponding to the amide I mode (1,595–1,720 cm^{-1}) and amide III envelope (1,243–1,269 cm^{-1}).

Such simple analyses, however, ignore the complexity of interactions between multiple mineral environments present in native bone. Therefore, we also applied the multivariate technique, factor analysis, to Raman spectra of day-28 mineralized nodules. Factor analysis can be used to interpret the results of principal-component analysis, a multivariate technique used to

analyse large, complex data sets. Principal-component analysis generates 'principal components', which contain spectral features corresponding to the molecular species responsible for statistical variation between spectra. When applied to spectra of mineralized nodules, the principal components can be 'rotated' (linearly combined) to give 'factors' that describe the mineral and matrix environments in a sample[21]. The position and shape of the PO_4^{3-} ν_1 band in factors is especially important, as it can reveal changes in ionic substitution and mineral crystallinity. Native bone contains three distinct mineral environments: B-type carbonate-substituted apatite, with a PO_4^{3-} ν_1 peak between 955 and 959 cm^{-1}, crystalline non-substituted hydroxyapatite, with a peak between 962 and 964 cm^{-1}, and an amorphous phosphate species, with a peak between 945 and 950 cm^{-1} (ref. 21), which together contribute to bone's function.

Factor analysis of OB and MSC spectra each produced three mineral factors. The two dominant OB mineral factors describe a carbonate-substituted apatite (Fig. 4f) and a non-substituted, crystalline apatite (Fig. 4j). The third, minor OB mineral factor (Fig. 4l) indicates an amorphous phosphate species. Factor analysis of MSC nodules similarly yielded a carbonate-substituted apatite (Fig. 4g) and a non-substituted crystalline apatite (Fig. 4k) as the main mineral species. A less prominent amorphous phosphate species (Fig. 4m) was also present. In contrast, factor analysis of ESC spectra generated only two mineral factors: a primary mineral factor describing a lightly carbonated crystalline apatite (Fig. 4e), and a secondary, minor factor describing a more carbonated, less crystalline apatite (Fig. 4i). Raman spectra of synthetic carbonated hydroxyapatite (cHA) standards (Fig. 4h) showed marked similarities to the carbonate-substituted apatite mineral factor detected in spectra from all three cell types (Fig. 4e–g). These data suggest that OB and MSC nodules contain mineral environments that are similar to those observed in native bone, namely a combination of carbonate-substituted and crystalline non-substituted apatite, and amorphous phosphate species. In contrast, ESC nodules were dominated by a single mineral factor, which was similar to synthetic cHA, and failed to show the more complex interaction of mineral species observed in OB and MSC.

Typical measures used to assess bone quality as determined by univariate peak-area analysis also confirmed that the mineral in ESC nodules was different from that in OB, MSC and native bone. The mineral-to-matrix ratio, a measure of the PO_4^{3-} ν_1 peak area to that of the spectral region indicative of protein molecular vibrations (1,600–1,720 cm^{-1}), was significantly lower in ESC than OB, MSC or native bone ($p < 0.05$) (Fig. 3b). We also found that the carbonate-to-phosphate ratio, which measures substitution of carbonate into the apatite lattice, was significantly higher in ESC than in OB, MSC or native bone. Similarly, the degree of mineral crystallinity, calculated from the FWHM of the PO_4^{3-} ν_1 band, was significantly higher in ESC than in the other materials (lower FWHM). Taken together, these data suggest that, although ESC formed less mineral than OB and MSC, this mineral was more crystalline and had a higher degree of carbonate substitution.

ESC nodules differed from OB and MSC not only in their mineral, but also in their organic phase. Factor analysis distinguished matrix factors for ESC, OB and MSC nodules (Fig. 4a–c) that reflected their proteinaceous component, and all showed similarities to spectra of type-I collagen standards (Fig. 4d). Gene expression analyses, however, noted clear differences among the different cell types. *Col1a1*, the gene for type-I collagen, was expressed at a level two orders of magnitude lower in mature cultures of ESC compared with OB and MSC (Fig. 5d), and when we re-examined premineralization cultures, we found that ESC seemed not to differentiate to osteoblasts in great numbers at all. Day-14 ESC cultures did not stain positively for the transcription factor Runx2 (Fig. 5a), an essential molecular switch for bone formation[22],

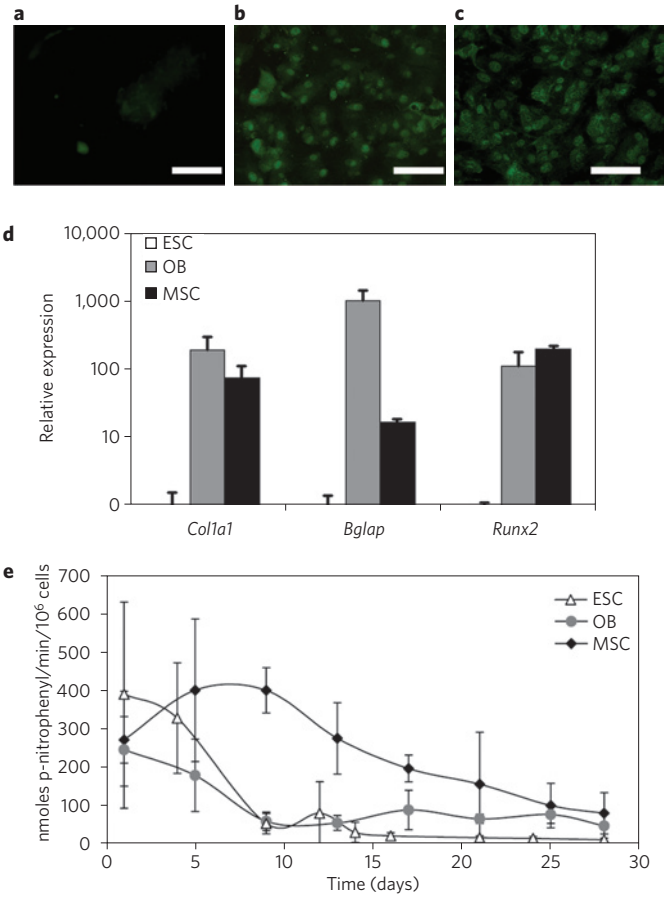

Figure 5 | Immunostaining, gene expression and alkaline-phosphatase (ALP) evidence of osteoblastic differentiation. a–c, Fluorescence micrographs showing immunostaining against transcriptional factor Runx2, an early marker for osteoblastic differentiation, in ESC, OB and MSC, respectively, after 14 days in culture. Notice that bright staining is localized to cell nuclei in OB and MSC whereas only diffuse stain is evident in ESC. The scale bar in **a**, **b** and **c** is 200 μm. **d**, Mean relative expression (and s.d.) as determined by quantitative RT-PCR of osteogenic genes *Bglap* (osteocalcin) and *Col1a1* (type-I collagen) in mature mineralized cultures, and *Runx2* in premineralization cultures of ESC, OB and MSC ($n \geq 3$). **e**, ALP activity (mean activity ± s.d.) as measured by the production of *p*-nitrophenyl per minute per 10^6 cells in cultures of ESC, OB and MSC over 28 days in culture.

whereas OB and MSC did (Fig. 5b,c). Real-time RT-PCR confirmed that *Runx2* expression in premineralized OB and MSC was 109 and 199 (respectively) times higher than that observed in ESC (Fig. 5d). The bone-specific protein osteocalcin, a late marker of osteoblast differentiation, similarly indicated limited osteoblastic differentiation in ESC. *Bglap*, the gene for osteocalcin, was expressed at levels 1,035 and 17 times higher in mature cultures of OB and MSC, respectively (Fig. 5d), compared with ESC.

To better understand mineral formation within nodules, we also carried out ultrastructural analysis. Bright-field transmission electron microscopy (TEM) revealed nodules to be multilayered structures containing cells and a partially mineralized ECM (Fig. 6a,b and Supplementary Fig. S2). Selected-area electron diffraction confirmed mineralized regions in both ESC and OB to be crystalline hydroxyapatite (Fig. 6a,b, insets)[23]. The ECM of OB nodules was composed of banded fibrils (Fig. 6e) with average diameters of 64.6 ± 9.8 nm and a periodicity of 60.2 ± 1.2 nm, which is similar to reported values for mammalian collagen[24]. Mineral formation in OB nodules also seemed to be mediated by calcium- and phosphate-containing (confirmed by EDX) matrix

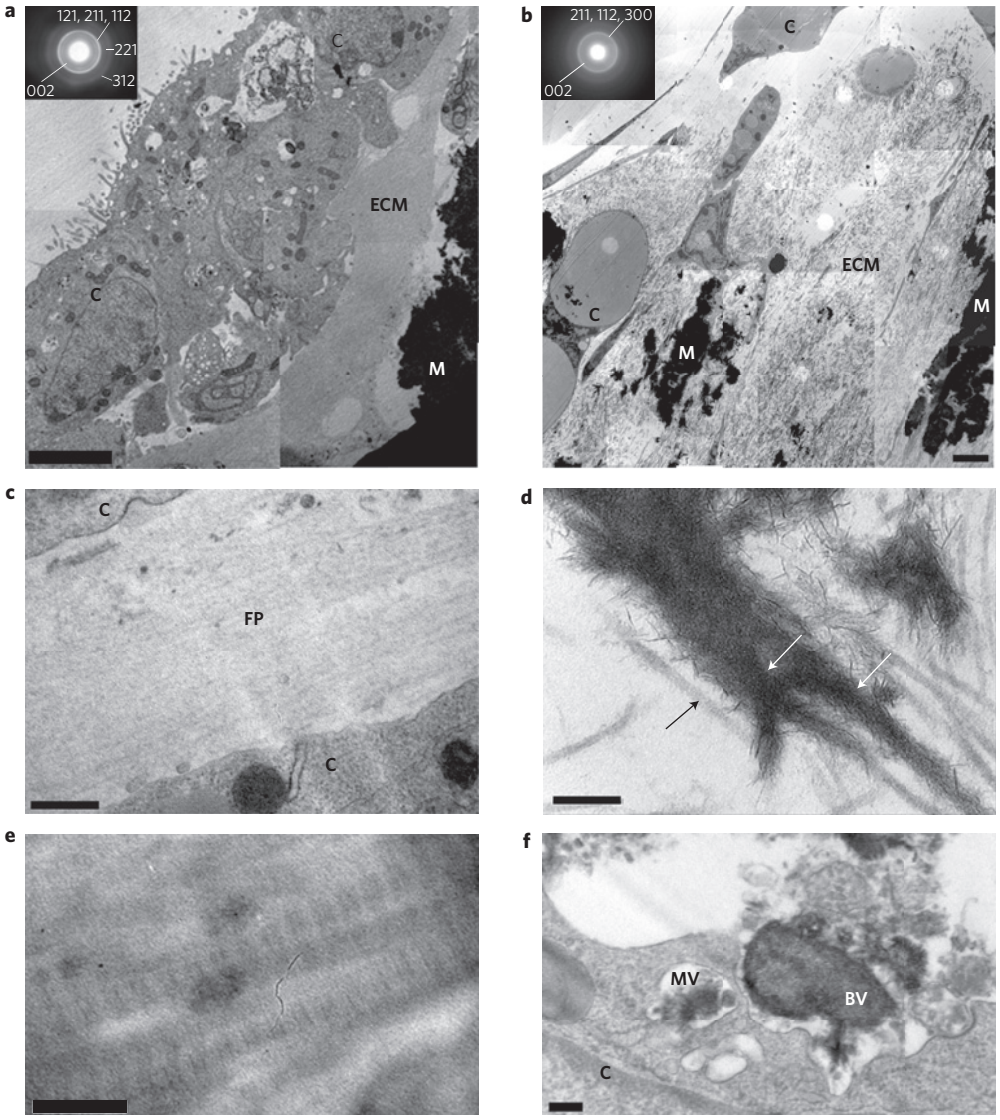

Figure 6 | TEM micrographs of mineralized nodules formed after 28 days in culture. a, Cross-section through an ESC nodule. A layer of cells is visible across the top of the nodule as indicated by **C**. The middle layer is composed of extracellular matrix (**ECM**). A dense layer of mineral (**M**) is also visible. The inset shows the selected-area electron diffraction pattern of the dense mineral portion of the nodule and is indicative of hydroxyapatite. **b**, Micrograph of a cross-section through an OB nodule. Cells are indicated by **C** and dense mineral by **M**. Fibrous **ECM** is also apparent. Selected-area electron diffraction of dense areas (inset) is indicative of hydroxyapatite. The scale bar in **a** and **b** is 4 μm. **c**, Higher-magnification image of fibrous protein (**FP**) between cells (**C**) in an ESC nodule. Note that the protein lacks the characteristic banding present in mammalian collagen. Scale bar = 0.5 μm. **d**, Micrograph showing unmineralized (black arrow) and mineralized banded fibrous proteins (white arrows) in OB nodules. **e**, Higher-magnification TEM micrograph of the ECM of OB nodules showing banding of fibrous proteins typical of mammalian collagen. **f**, Micrograph of matrix vesicle (**MV**) containing needle-like apatite crystals inside a cell (**C**) within an OB nodule. A bursting matrix vesicle (**BV**) is also visible. The scale bar in **d**, **e** and **f** is 0.2 μm.

vesicles created intracellularly, which were observed bursting into the extracellular space, releasing their apatite crystallites (Fig. 6f). Although they lacked the collagen–mineral organization of native bone, these mineral crystallites were observed to associate with collagen fibrils (Fig. 6d). Conversely, the ECM of ESC nodules was dominated by fibrous structures with a diameter of 39.6 ± 4.6 nm (Fig. 6c). These fibrils rarely showed the characteristic banding pattern of collagen, and mineral formation was only occasionally observed to take place in intracellularly formed, apatite-containing vesicles. Furthermore, we failed to detect apatite crystallites associated with protein fibrils in ESC nodules; it instead formed in discrete clusters. Indeed, when we examined their mechanical behaviour by nanoindentation, we found that ESC nodules were significantly ($p < 0.001$) less stiff than those formed from OB or MSC ($0.11 \pm 0.07\ \mu N\ nm^{-1}$ ESC; $7.3 \pm 4.3\ \mu N\ nm^{-1}$ OB; $3.0 \pm 3.7\ \mu N\ nm^{-1}$ MSC; Supplementary Fig. S3), suggesting that the lack of connectivity between the mineral and fibrous proteins of the ESC nodules significantly impacted their mechanical properties.

Taken together, these results suggest that a mechanism other than osteoblast-mediated mineralization of collagen fibrils was in large part responsible for the 'bone nodules' observed in ESC, and therefore the mineral may have been, at least in part, dystrophic[25]. Dystrophic mineral has been previously described[26] and can form when inorganic phosphates from locally high levels of ALP activity precipitate with calcium ions in cell culture media. ALP activity per cell was high in proliferating cultures at early time points and decreased as cultures mineralized, as has been previously reported[27] (Fig. 5e). ALP activity in ESC was similar to that observed in OB and MSC. However, as differentiating ESC expressed osteoblastic genes

at levels nearly two orders of magnitude lower than OB and MSC, this result suggests that non-osteoblastic cells in the ESC population also produce ALP, facilitating deposition of dystrophic mineral. Indeed, we suggest that it is likely that much of the ARS staining of ESC nodules in this and other studies stems from this and not solely through the activity of mineralizing osteoblasts.

We have shown that OB and MSC form a type-II collagen intermediary before mineralization. This transition resembles endochondral ossification, the process by which long bones in the embryonic skeleton develop by first forming a cartilage template. Although an analogous process *in vitro* may seem unlikely, as embryonic bone development is strictly delineated depending on skeletal location, there is evidence to suggest that bone progenitors are actually fairly plastic[28]. As such, calvarial osteoblasts that would normally form bone by intramembranous ossification (the process by which flat bones in the skull form by depositing mineral directly on a collagenous ECM) may be able to take a different differentiation pathway. For example, the application of mechanical forces is known to favour endochondral versus intramembranous ossification, regardless of how the bone would normally form[29]. Minor changes in the presence of growth factors during development also have an influence. Transgenic mice that express fibroblast growth factor 9 in the cranial mesenchyme, for example, form cranial bone by endochondral rather than intramembranous ossification[30].

The type-II collagen detected in OB and MSC cultures, however, did not persist. The cells instead expressed osteogenic genes and created a proteinaceous ECM that mineralized over time, as has been noted in native bone. Differentiating ESC, conversely, failed to express osteogenic genes at levels noted in OB and MSC, and the mineral in ESC nodules failed to closely associate with matrix proteins. The poor composite structure in ESC nodules also impacted their mechanical properties, as nanoindentation determined they were significantly less stiff than OB and MSC nodules. These results suggest that standard protocols widely reported to direct the differentiation of ESC to osteoblasts that form a bone-like material fail to do so in significant numbers and/or fail to prevent non-osteoblastic differentiation. This may significantly impact the outcome of bone regenerative therapies, regardless of how long the cells persist after implantation. In *in vivo* models, osteogenic scaffolds seeded with dermal fibroblasts yielded similar results to no-cell controls (that is, lack of tissue formation)[31], suggesting that osteogenic cells are an essential component of bone regeneration constructs. Moreover, although the need for differentiation *in vitro* before implantation is controversial, some convincing reports demonstrate improved tissue outcomes when cells are cultured in the presence of tissue-stimulating factors before implantation, even in so-called niches, where factors that presumably stimulate appropriate differentiation are present[32].

OB and MSC nodules contained three distinct mineral environments, which in native bone are thought to indicate continued remodelling and reflect a combination of older and newer bone in small bone-forming units called osteons[33]. Multiple mineral environments in native bone are also reflected in its carbonate-to-phosphate ratio and crystallinity, as both increase with increasing tissue age[34]. ESC nodules lacked complex combinations of multiple mineral environments, were significantly more crystalline and had a significantly higher carbonate-to-phosphate ratio than those formed from OB and MSC. This suggests that mineral in ESC nodules more closely resembled the crystalline, highly carbonated mineral in older bone than that in normal bone. Not surprisingly, changes in mineral have been shown to affect bone's mechanical properties. Akkus *et al.* among others have correlated increasing carbonate substitutions and crystallinity with increasing age and deteriorating mechanical properties[35,36]. Similarly, spectroscopic studies of osteoporotic bone reveal a narrower range in parameters such as crystallinity and carbonate-to-phosphate ratio compared with normal bone, suggesting that the combination of multiple mineral environments contributes to mechanical function[37]. Given the well-documented effects associated with minor changes in bone-mineral environments, our results highlight the importance of precisely matching the biochemical and material characteristics of engineered bone to those of the native tissue.

A fundamental hurdle in taking regenerative medicine from the laboratory to the clinic is determining whether cells cultured *in vitro* truly mimic their counterparts in the healthy native tissue. Here we detail the processes by which cells from three sources form bone-like material *in vitro* and highlight the differences between them. OB and MSC were successfully able to create a material with many hallmarks of native bone, whereas that formed by ESC differed in its composition, stiffness, nanolevel architecture and development. Only by assessing the material with both biological and materials-based techniques could these differences, which will probably have a significant impact on clinical success, be discerned.

Methods

Cell culture. ESC, OB and MSC were routinely cultured and differentiated in medium containing ascorbic acid, β-glycerophosphate and dexamethasone as described in the Supplementary Methods.

Raman standards. Type-I collagen from bovine tendon and type-II collagen from chicken sternal cartilage were purchased from Sigma. Fresh calvarial mouse bone samples were obtained from adult mice; spectral measurements were made within two hours. cHA was prepared by a precipitation route[38].

Alizarin Red S staining. Day-28 cultures were rinsed with PBS, fixed for 20 min in formalin, rinsed, stained for 10 min in 2% (w/v) ARS in deionized H_2O, rinsed again and air dried[39]. Stained plates were viewed using phase contrast and epifluorescence microscopy (excitation 510–560 nm, emission >590 nm).

Scanning electron microscopy and energy-dispersive X-ray spectroscopy. Day-28 nodules were fixed, dried and gold or carbon coated and viewed using a Leo 1525 Gemini scanning electron microscope with an EDX detector as described in Supplementary Methods.

Micro-Raman spectroscopy. Raman spectra were collected from live cell cultures maintained in DMEM with 1× penicillin/streptomycin at 37 °C. Spectra were measured with a Renishaw InVia spectrometer connected to a Leica microscope and equipped with a 785 nm line-focus laser (120 mW before objective) with an elliptical beam profile. Refer to Supplementary Methods for a detailed description of spectra collection and spectral analysis.

Immunocytochemistry. After 14 days, some cultures were rinsed with PBS, fixed in a solution of 4% (w/v) paraformaldehyde (Sigma) in deionized H_20 for 20 min and stained with antibodies to type-II collagen (R&D Systems; 1:40) or Runx2 (Santa Cruz Biotechnology; 1:80). Primary antibodies were detected with secondary antibodies conjugated to FITC and viewed using epifluorescence microscopy.

Quantitative real-time RT-PCR. Cells were detached from culture plates at the indicated time points and snap frozen. RNA was extracted, reverse transcribed and amplified as described in the Supplementary Methods. Sequences and cycling conditions for primers to *Gapdh*, *Bglap*, *Runx2*, *Sox9*, *Col1a1* and *Col1a2* are given in Supplementary Table S1. Relative expression was calculated using the Pfaffel method[40]. As the onset of mineralization was somewhat variable, expression levels combine data from at least three time points in the appropriate range. Data are presented as the mean relative expression ±standard deviation compared with the expression of ESC at the same time point.

Transmission electron microscopy and selected area electron diffraction. Day-28 nodules were prepared for TEM through either a standard protocol for analysis of cell structure or an anhydrous procedure for examination of mineral structure and chemistry. 70 nm sections were viewed on a Jeol 2000 as described in Supplementary Methods.

Nanoindentation mechanical testing. Stiffness of day-28 nodules was assessed by displacement-controlled nanoindentation on a Hysitron UBI nanoindentor as described in Supplementary Methods.

Alkaline-phosphatase activity. ESC, OB and MSC cultures were lysed by three freeze–thaw cycles in dH_2O. ALP activity was assessed using p-nitrophenyl phosphate as a substrate (Sigma); the absorbance of its product, p-nitrophenyl, was measured at 405 nm. ALP activity was normalized to cell number, which was quantified by measuring the activity of the stable cytosolic enzyme lactate dehydrogenase with a CytoTox96 assay (Promega).

Received 12 February 2009; accepted 25 June 2009; published online 26 July 2009

References

1. Giannoudis, P. V., Dinopoulos, H. & Tsiridis, E. Bone substitutes: An update. *Injury* **36** (Suppl 3), S20–S27 (2005).
2. Friedlaender, G. E. Immune responses to osteochondral allografts. Current knowledge and future directions. *Clin. Orthop.* **174**, 58–68 (1983).
3. Patel, R. & Trampuz, A. Infections transmitted through musculoskeletal-tissue allografts. *N. Engl. J. Med.* **350**, 2544–2546 (2004).
4. Evans, M. J. & Kaufman, M. H. Establishment in culture of pluripotential cells from mouse embryos. *Nature* **292**, 154–156 (1981).
5. Thomson, J. A. *et al.* Embryonic stem cell lines derived from human blastocysts. *Science* **282**, 1145–1147 (1998).
6. Alper, J. Geron gets green light for human trial of ES cell-derived product. *Nature Biotech.* **27**, 213–214 (2009).
7. Gruen, L. & Grabel, L. Concise review: Scientific and ethical roadblocks to human embryonic stem cell therapy. *Stem Cells* **24**, 2162–2169 (2006).
8. Litinski, V. & Kim, L. *Regenerarive Medicine Industry Briefing* (MaRS Venture Group, 2008).
9. Lewandrowski, K. U., Gresser, J. D., Wise, D. L. & Trantol, D. J. Bioresorbable bone graft substitutes of different osteoconductivities: A histologic evaluation of osteointegration of poly(propylene glycol-co-fumaric acid)-based cement implants in rats. *Biomaterials* **21**, 757–764 (2000).
10. Buttery, L. D. *et al.* Differentiation of osteoblasts and *in vitro* bone formation from murine embryonic stem cells. *Tissue Eng.* **7**, 89–99 (2001).
11. Ecarot-Charrier, B., Glorieux, F. H., van der Rest, M. & Pereira, G. Osteoblasts isolated from mouse calvaria initiate matrix mineralization in culture. *J. Cell Biol.* **96**, 639–643 (1983).
12. Schoeters, G. E., de Saint-Georges, L., Van den Heuvel, R. & Vanderborght, O. Mineralization of adult mouse bone marrow *in vitro*. *Cell Tissue Kinet.* **21**, 363–374 (1988).
13. Shimko, D. A., Burks, C. A., Dee, K. C. & Nauman, E. A. Comparison of *in vitro* mineralization by murine embryonic and adult stem cells cultured in an osteogenic medium. *Tissue Eng.* **10**, 1386–1398 (2004).
14. Stevens, M. M. & George, J. H. Exploring and engineering the cell surface interface. *Science* **310**, 1135–1138 (2005).
15. Tzaphlidou, M. & Zaichick, V. Sex and age related Ca/P ratio in cortical bone of iliac crest of healthy humans. *J. Radioanal. Nucl. Chem.* **259**, 347–349 (2004).
16. Swain, R. J. & Stevens, M. M. Raman microspectroscopy for non-invasive biochemical analysis of single cells. *Biochem. Soc. Trans.* **35**, 544–549 (2007).
17. Krishna, C. M. *et al.* Micro-Raman spectroscopy for optical pathology of oral squamous cell carcinoma. *Appl. Spectrosc.* **58**, 1128–1135 (2004).
18. Diem, M., Romeo, M., Boydston-White, S., Miljkovic, M. & Matthaus, C. A decade of vibrational micro-spectroscopy of human cells and tissue (1994–2004). *Analyst* **129**, 880–885 (2004).
19. Bi, W., Deng, J. M., Zhang, Z., Behringer, R. R. & de Crombrugghe, B. Sox9 is required for cartilage formation. *Nature Genet.* **22**, 85–89 (1999).
20. Carden, A. & Morris, M. D. Application of vibrational spectroscopy to the study of mineralized tissues (review). *J. Biomed. Opt.* **5**, 259–268 (2000).
21. Tarnowski, C. P., Ignelzi, M. A. Jr & Morris, M. D. Mineralization of developing mouse calvaria as revealed by Raman microspectroscopy. *J. Bone Miner. Res.* **17**, 1118–1126 (2002).
22. Ducy, P., Zhang, R., Geoffroy, V., Ridall, A. L. & Karsenty, G. Osf2/Cbfa1: A transcriptional activator of osteoblast differentiation. *Cell* **89**, 747–754 (1997).
23. Porter, A. E., Patel, N., Skepper, J. N., Best, S. M. & Bonfield, W. Effect of sintered silicate-substituted hydroxyapatite on remodelling processes at the bone-implant interface. *Biomaterials* **25**, 3303–3314 (2004).
24. Ushiki, T. Collagen fibers, reticular fibers and elastic fibers. A comprehensive understanding from a morphological viewpoint. *Arch. Histol. Cytol.* **65**, 109–126 (2002).
25. Bonewald, L. F. *et al.* von Kossa staining alone is not sufficient to confirm that mineralization *in vitro* represents bone formation. *Calcif. Tissue Int.* **72**, 537–547 (2003).
26. Boyan, B. D., Schwartz, Z. & Boskey, A. L. The importance of mineral in bone and mineral research. *Bone* **27**, 341–342 (2000).
27. Aubin, J. E., Liu, F., Malaval, L. & Gupta, A. K. Osteoblast and chondroblast differentiation. *Bone* **17**, 77S–83S (1995).
28. Fang, J. & Hall, B. K. Chondrogenic cell differentiation from membrane bone periostea. *Anat. Embryol. (Berl)* **196**, 349–362 (1997).
29. Shapiro, F. Bone development and its relation to fracture repair. The role of mesenchymal osteoblasts and surface osteoblasts. *Eur. Cell Mater.* **15**, 53–76 (2008).
30. Govindarajan, V. & Overbeek, P. A. FGF9 can induce endochondral ossification in cranial mesenchyme. *BMC Dev. Biol.* **6**, 7 (2006).
31. Kim, S. *et al. In vivo* bone formation from human embryonic stem cell-derived osteogenic cells in poly(d,l-lactic-co-glycolic acid)/hydroxyapatite composite scaffolds. *Biomaterials* **29**, 1043–1053 (2008).
32. Hwang, N. S. *et al. In vivo* commitment and functional tissue regeneration using human embryonic stem cell-derived mesenchymal cells. *Proc. Natl Acad. Sci. USA* **105**, 20641–20646 (2008).
33. Boskey, A. & Pleshko Camacho, N. FT-IR imaging of native and tissue-engineered bone and cartilage. *Biomaterials* **28**, 2465–2478 (2007).
34. Boskey, A. Bone mineral crystal size. *Osteoporos. Int.* **14** (Suppl 5) S16–S20; discussion S20-S11 (2003).
35. Akkus, O., Adar, F. & Schaffler, M. B. Age-related changes in physicochemical properties of mineral crystals are related to impaired mechanical function of cortical bone. *Bone* **34**, 443–453 (2004).
36. Yerramshetty, J. S. & Akkus, O. The associations between mineral crystallinity and the mechanical properties of human cortical bone. *Bone* **42**, 476–482 (2008).
37. Gadeleta, S. J. *et al.* A physical, chemical, and mechanical study of lumbar vertebrae from normal, ovariectomized, and nandrolone decanoate-treated cynomolgus monkeys (*Macaca fascicularis*). *Bone* **27**, 541–550 (2000).
38. Sogo, Y., Ito, A., Yokoyama, D., Yamazaki, A. & LeGeros, R. Z. Synthesis of fluoride-releasing carbonate apatites for bone substitutes. *J. Mater. Sci. Mater. Med.* **18**, 1001–1007 (2007).
39. Syftestad, G. T., Weitzhandler, M. & Caplan, A. I. Isolation and characterization of osteogenic cells derived from first bone of the embryonic tibia. *Dev. Biol.* **110**, 275–283 (1985).
40. Pfaffl, M. W. A new mathematical model for relative quantification in real-time RT-PCR. *Nucleic Acids Res.* **29**, e45 (2001).
41. Carter, E. A. & Edwards, H. G. M. *Infrared and Raman Spectroscopy of Biological* (Dekker, 2001).
42. Notingher, I., Jell, G., Lohbauer, U., Salih, V. & Hench, L. L. *In situ* non-invasive spectral discrimination between bone cell phenotypes used in tissue engineering. *J. Cell. Biochem.* **92**, 1180–1192 (2004).

Acknowledgements

The authors would like to thank the EPSRC for funding, R. Carzaniga of the Electron Microscopy Centre, Imperial College London, for invaluable assistance with TEM and N. Walters for laboratory support. We are also grateful to R. Hill for help with the hydroxyapatite standard. R.J.S. gratefully acknowledges funding from the Rothermere Foundation, the National Science and Engineering Research Council Canada and the Canadian Centennial Scholarship Fund. N.D.E. was supported by a career development fellowship in stem cell research from the Medical Research Council, UK.

Author contributions

E.G. carried out the cell culture work and the ALP assays and wrote the majority of the manuscript. R.J.S. carried out the Raman measurements and spectral processing and analysis and also contributed to manuscript writing and revision. N.D.E contributed some cell culture work, immunostaining results and the quantitative PCR data and helped with manuscript revision. G.J. and M.D.B carried out the SEM imaging and some TEM preparation. G.J. also contributed to manuscript revision. S.B. carried out the majority of the TEM imaging. T.A.V.S. and M.L.O. carried out the nanoindentation testing. A.P. helped with the TEM imaging and manuscript revision. M.M.S. was involved in study design, supervision of the work and manuscript revision.

Additional information

Supplementary information accompanies this paper on www.nature.com/naturematerials. Reprints and permissions information is available online at http://npg.nature.com/reprintsandpermissions. Correspondence and requests for materials should be addressed to M.M.S.